



CHORUS

This is the accepted manuscript made available via CHORUS. The article has been published as:

Observation of Shell Structure, Electronic Screening, and Energetic Limiting in Sparks

A. Bataller, S. Putterman, S. Pree, and J. Koulakis

Phys. Rev. Lett. **117**, 085001 — Published 19 August 2016

DOI: [10.1103/PhysRevLett.117.085001](https://doi.org/10.1103/PhysRevLett.117.085001)

Observation of Shell Structure, Electronic Screening, and Energetic Limiting in Sparks

A. Bataller,¹ S. Putterman,¹ S. Pree,¹ and J. Koulakis¹

*¹Department of Physics and Astronomy,
University of California, Los Angeles,
Los Angeles, California 90095, USA**

Abstract

We study the formation of micron-sized spark discharges in high-pressure xenon on the nanosecond timescale. The spark's energy per length is measured through the expansion dynamics of the generated shockwave, and is observed to scale linearly with the spark radius. At the same time, the surface temperature of the spark channel remains constant. Together, these observations allow us to conclude that the spark channel, up to 40 μm in overall radius, is actually an energetically hollow shell about 20 μm thick. Further, the energy per nucleus in the shell is about 15 eV, independent of size and density. To reconcile these findings with the opacity to visible light, we appeal to collective screening processes that dramatically lower the effective ionization potential, allowing a much higher electron density than is expected. Thus nanosecond measurements of sparks provide access to the thermodynamics and kinetics of strongly correlated plasmas.

PACS numbers:

Examples of systems that become dense plasmas when driven off-equilibrium are high-voltage electrical breakdown (spark discharges [1]), ultra-fast laser breakdown [2], adiabatic heating of gases in shock fronts [3, 4], and bubble implosions (sonoluminescence [5]). As these systems are driven harder, their brightness is observed to saturate. This luminosity saturation, first recognized by Glaser [6, 7], exists over a wide range of parameter space. Although this phenomenon has been known for over 60 years, its explanation is still in contention [8, 9]. Attempts to find the thermodynamic and kinetic origins of this effect are shrouded by the simultaneous onset of opacity at unexpectedly low temperatures and energy inputs. We use the acoustic and hydrodynamic response of the dense plasma expansion to peek inside of dense xenon sparks which are formed in a nanosecond - fast compared to hydrodynamic timescales. We find that the spark current flows in a shell structure where the energy per atom is a constant, independent of both the absorbed energy (or spark diameter) and the initial density. Furthermore, the surface temperature remains constant for 25 ns, a period much longer than the energy input time. Opacity is established in under 1 ns, and this property of the plasma is due to processes that strongly reduce the ionization potential. The experimental techniques presented in this Letter enable ultrafast measurements spanning isochoric to steady-state timescales, and establish a unified set of data for energetics, potential lowering, electronic screening, and hydrodynamic motion. Dense plasmas in the parameter space described here are useful as ultra-violet sources, rapid optical switches with broadband functionality extending to the ultra-violet, and precision discharge machining tools.

Luminosity saturates at a brightness corresponding to blackbody emission at a gas-dependent temperature T_{sat} . The saturation occurs in both time and space as shown by the streak image in Fig. 1(a). The image was taken along a radial cross-section (streak slit indicated in Fig. 2(a)) for a spark discharge in 42 bar xenon. In Fig. 1(c), a temporal lineout centered on the spark channel shows that the gas breakdown process forms in <1 ns with a rapidly rising intensity indicated at $t = 0$ ns. The luminosity saturates at $5 \pm 0.5 \mu\text{W}/\text{nm} \mu\text{m}^2$ within the first nanosecond and continues for 20 – 25 ns. During this time, the luminous profile (Fig. 1(d)) is well fit to a flattop function (super-Gaussian), indicating saturation in space as well.

Hydrodynamic analysis of Fig. 1 is the basis for insights regarding the interior of the blackbody emitter. This image was taken with a Hamamatsu streak camera aligned to a

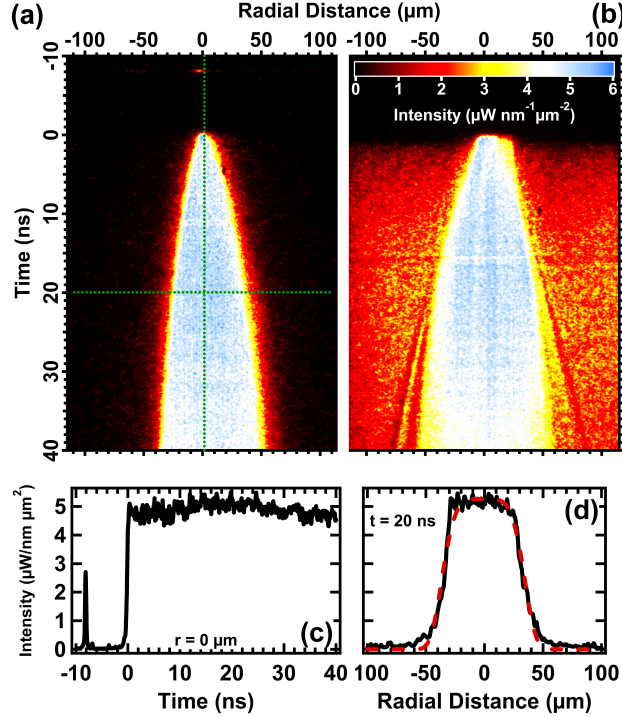


Figure 1: Time-resolved radial cross-section of a spark discharge in 42 bar (a) and 10 bar (b) Xe. In (b), a backlight renders the emitted shockwave visible. Temporal (c) and radial (d) line-outs, whose position is indicated by the green dotted lines in (a), reveal brightness saturation occurring both in time and space. A weak femtosecond laser pulse initiates the discharge, indicated by emission at -10 ns in (a) and (c). Red-dashed curve in (d) is the best-fit super-Gaussian.

10 \times long-range Mitutoyo microscope objective as shown in Fig. 2(b). A 550 nm band-pass filter (10 nm bandwidth) was placed between the objective and streak camera, whose spectral intensity was cross-calibrated with the fiber spectrometer system (Fig. 2(b)). Details of the pressure chamber and electrical circuit used to generate the discharges can be found elsewhere [10]. Briefly, spark discharges were generated in a stainless-steel pressure chamber between 80 μm diameter tungsten needles that were dulled through a series of spark discharges. A 50 Ω coaxial cable attached to the electrodes through a feedthrough in the chamber walls was charged to 5 kV through a 250 Ω isolation resistor. In contrast to [10] where a fast-rise-time switch was used to charge the cable to a voltage surpassing the breakdown threshold, here the gap length is increased so that the potential stays below threshold. The breakdown is then initiated with a weak ($< \mu\text{J}$) femtosecond laser pulse focused between the electrodes. This represents a significant advancement in spark trigger-

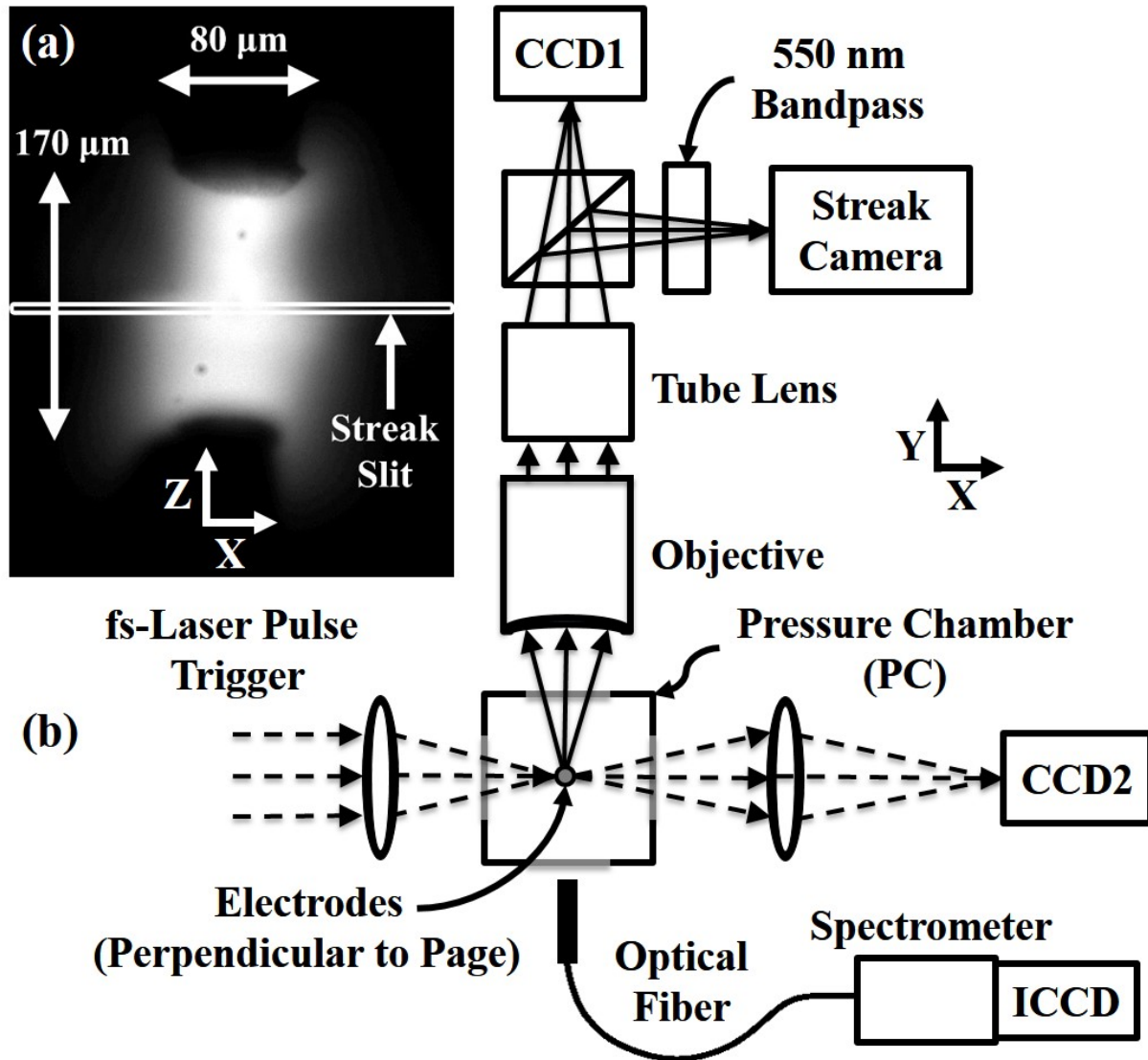


Figure 2: Block diagram (b) of the system used to study spark discharges in 10-42 bar Xe. (a) is a time-integrated photograph of a single spark event in 20 bar Xe as captured by CCD1. The pressure chamber contains two $80\ \mu\text{m}$ diameter tungsten needles (perpendicular to the plane of the block diagram and seen as silhouettes in (a)), held $170\ \mu\text{m}$ apart and charged to 5 kV. CCD1 and CCD2 are used for alignment and diagnostics. Sub-nanosecond dynamics are resolved by the streak camera (Fig.1), which images a narrow band across the spark width, indicated as “Streak Slit” in (a).

ing that lowers timing jitter by over an order of magnitude and makes possible ultra-fast measurements on the micron scale.

Importantly, the luminosity-saturated sparks we present are in a different regime than those considered by others [6, 7], and particularly Yusupaliev, whose brightness-saturation theory [11] assumes that power continues to drive the system well after the hydrodynamic shockwave has been formed. In contrast, we consider sparks whose energy source has been exhausted before hydrodynamic expansion even begins, and therefore the atomic density remains equal to the ambient. We achieved this regime by relying purely on the capacitive energy stored within our drive cable and the parasitics of the chamber, which discharge quickly. There remains an opportunity for a luminosity-saturation theory on such rapid timescales.

A key feature of the luminosity saturation regime is the blackbody nature of the plasma emission. The flattop radial profile observed in Fig. 1(d) is suggestive of this, as a blackbody is a Lambertian radiator. To confirm the presence of blackbody radiation and the gas-dependent T_{sat} , calibrated, time-resolved spectra were obtained for xenon spark discharges. Indeed, Fig. 3 shows spectrum taken at 3 ns matching a 29 000 K blackbody, in agreement with previous studies of xenon discharges [12, 13]. Along with increasing power input, T_{sat} can also be reached by increasing gas pressure as long as the power input is above a minimum value [14]. Fig. 3 demonstrates this trend as the spectral intensity reaches its limiting value between 10 and 20 bar. Spectrum was acquired with a fiber-coupled ICCD spectrometer (Princeton Instruments), where individual spark emission spectra were recorded in 1 ns exposures, averaged, and reconstructed as a function of discharge time. The spectra were then divided by their averaged plasma dimensions from corresponding streak images and electrode separation. The spectrometer system was calibrated to an uncertainty of 10% using deuterium and tungsten sources, limiting the blackbody fitting parameters to only temperature and allowing quantitative radiative analysis.

Fitting radial lineouts to a super-Gaussian function $I(x) = I_0 \exp(-2 |(\frac{x-x_0}{\sigma})^n|)$ at each time point (red-dashed curve in Fig. 1(d)) provides the spark channel radius (half-width-at-half-max) over time (Fig. 4). The spark expansion dynamics can be categorized into four temporal phases referenced to the onset of light emission:

1. **Leader Phase ($t < 0$ ns)** - This is the earliest phase of the discharge where seed ions created from the weak femtosecond laser pulse (Figs. 1(a)&(c)) migrate and collide

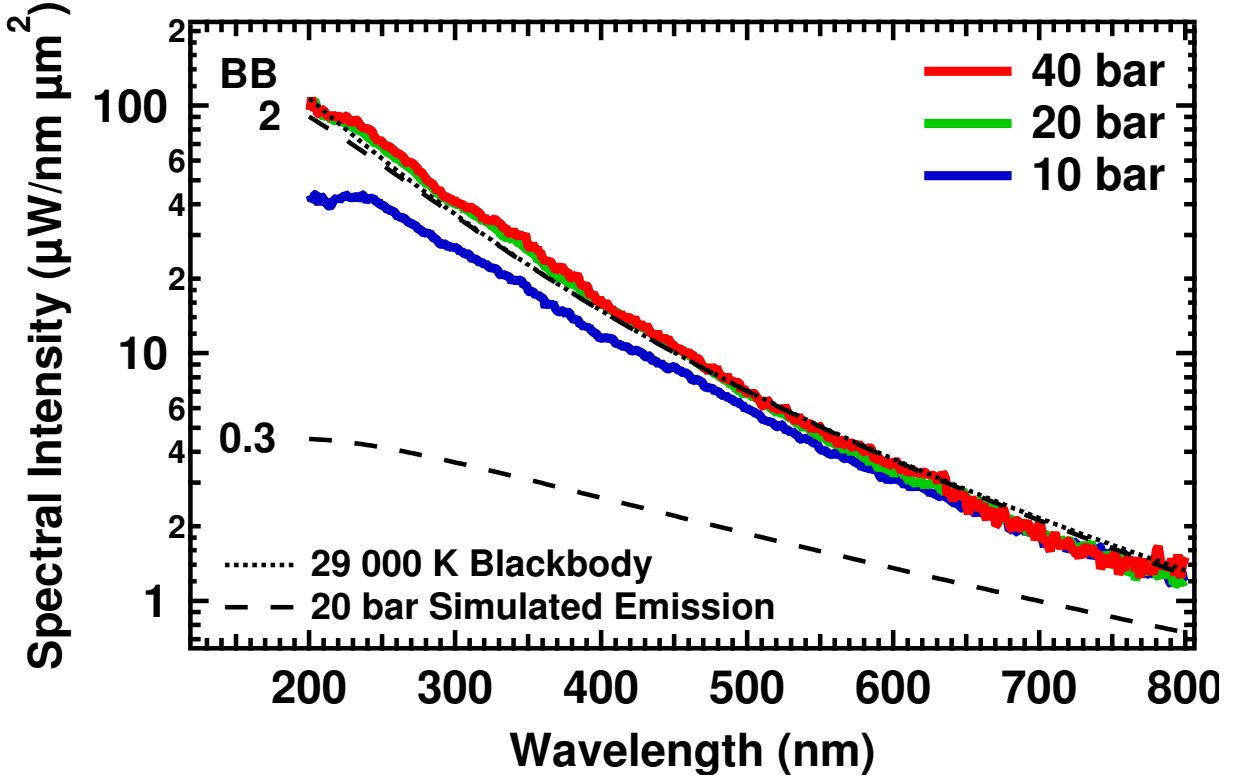


Figure 3: Absolute spectral intensity of Xe discharges at 3 ns for various static pressures. Spectral saturation throughout the measured spectrum occurs for pressures >10 bar and are well-fit to a 29 000 K blackbody spectrum (dotted). Simulated spectra (dashed) at 20 bar were calculated for various levels of ionization ($Z = 0.3$ and 2) using Eq. 7 at $T_{sat} = 29\,000$ K and $l = 40\ \mu\text{m}$.

with the cathode. Once the secondary emission initiates a cascade, a plasma leader races across the electrode gap, and a luminous spark channel becomes visible [15]. Explosive electron emission [16] represents a possible mechanism for the initial cascade, as suggested by the cathode’s micron-scale radius of curvature, the small material removal after discharge ($\sim 1\ \text{nm}/\text{shot}$), the nanosecond delay before light emission, and the high electric field and current density.

2. **Ionization Wave Phase ($0 < t < 3\ \text{ns}$)** - Once the spark leader has bridged the electrodes, the channel diameter grows rapidly as circuit energy pours into heating and creating a larger plasma. This phase is likely an ionization wave front, considering the fast expansion speed ($>5\ \text{km}/\text{s}$) and the absence of a radiated shock front subsequent to its rapid deceleration around 3 ns. During this phase, the plasma reaches T_{sat} .

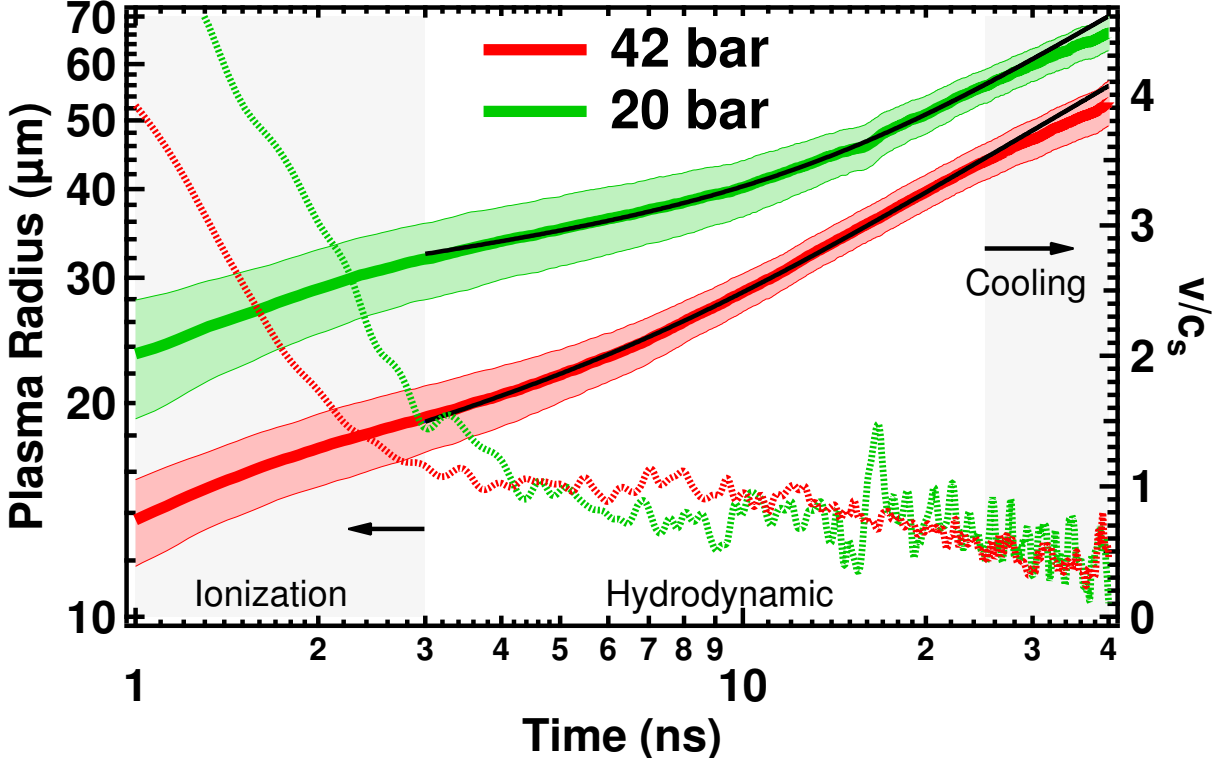


Figure 4: Plasma radius (solid) and velocity (dotted) as a function of time for 20 and 42 bar discharges. Discharge sizes varied from shot-to-shot within the range indicated by the shaded regions bounding the radius curves. The radial expansion is fit (black) to Eq. 1 between 3 – 25 ns. A shockwave is released from the plasma surface between 20-25 ns as indicated in the shaded region. The plasma velocity is shown normalized to the isothermal speed of sound of a 29 000 K gas ($c_s = \sqrt{kT_{sat}/M_{Xe}} = 1.36 \mu\text{m/ns}$).

3. **Hydrodynamic Phase ($3 < t < 25 \text{ ns}$)** - Additional heating is limited by the small stray circuit capacitance and the sharply-dropping plasma resistance. Once power input has ended, the channel undergoes a hydrodynamic expansion near the speed of sound of a 29 000 K xenon plasma. This phase ends when the plasma size is so large that the initial energy input can no longer sustain the expansion, ending with a radiated shock wave (Fig. 1(b)).
4. **Cooling Phase ($t > 25 \text{ ns}$)** - Lasting 100s of nanoseconds, this phase represents the spark’s death as the plasma cools off from T_{sat} to room temperature. During this phase, the plasma becomes dilute and optically thin.

We find the dynamics of the spark channel radius between 3–25 ns (Fig. 4) are well-described

by the function,

$$R(t) = A \exp\left(-\frac{t}{\tau}\right) + \sqrt{Bt}. \quad (1)$$

The second term captures the asymptotic behavior of a cylindrical shock as expected from the Sedov-Taylor self-similar solution, which assumes the initial energy input is a delta-function in time and the shock radius is much larger than the initial radius. Because the channel resistance drops rapidly, the vast majority of the energy deposition occurs in the first nanosecond. The initially rapid expansion of the channel diameter slows dramatically when the power input becomes negligible, as seen between 2 – 4 ns in the velocity curves of Fig. 4. Further expansion is driven by hydrodynamics rather than ionization, and the velocity flattens out at around the speed of sound. Additional evidence that further energy input is negligible is provided by the observation that changing the charging cable length does not affect the channel dynamics. We empirically insert the exponential term to account for the shock acceleration, and fit the radius-time curves during the hydrodynamic phase (3 – 25 ns) to Eq. 1 to extract the best-fit parameters A , τ , and B . We have also observed the shock post-separation with the use of a backlight (Fig 1(b)), and find that it continues to follow the \sqrt{t} expansion until the radius becomes comparable to the electrode distance, after which the shock becomes spherical.

Unit analysis and self-similar theory gives the coefficient B as being proportional to the half power of the energy per length E/L , over the mass density $\rho = n_0 M_{Xe}$, with the proportionality constant being a function of the adiabatic index γ [17, 18],

$$B^2 = \left[\frac{4(\gamma - 1)(\gamma + 1)^2}{\pi(3\gamma - 1)} \right] \frac{E}{L\rho} = f(\gamma) \frac{\pi R_0^2 \bar{\epsilon}}{M_{Xe}}, \quad (2)$$

$$\text{where } \bar{\epsilon} = \frac{2}{R_0^2} \int_0^{R_0} \epsilon(r) r dr, \quad (3)$$

is the spatial average of the energy per nucleus $\epsilon(r)$, over the initial radius R_0 , n_0 is the initial atomic density, and M_{Xe} is the atomic mass of xenon. R_0 is the radius of the spark channel after the majority of the energy has been deposited, i.e. after the ionization wave phase, but before the hydrodynamic expansion begins. This occurs at $t = 4$ (3) ns for 20 (42) bar, as that is when the velocity of the early, rapid expansion has dropped to approximately the speed of sound [31], and flattens off (Fig. 4). We use the shockwave asymptotic dynamics to back-out the energy absorbed by the spark, and then assign that energy to the number of particles in the initial channel volume. At 3 ns, the channel density is assumed uniform and

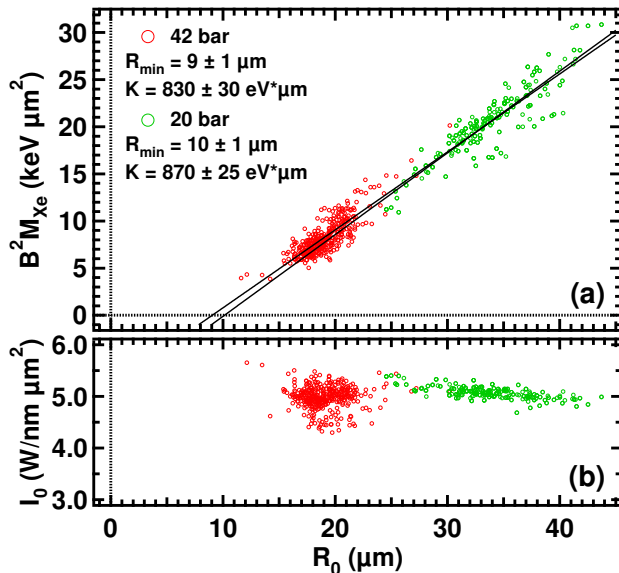


Figure 5: Scatter plots of (a) $B^2 M_{Xe}$ and (b) the brightness of the spark channel vs. the initial plasma radius for individual discharges at 20 and 40 bar. $B^2 M_{Xe}$ is proportional to $(R_0 - R_{min})$ and is pressure independent, while the surface brightness is independent of both spark size and pressure.

equal to the ambient density, as sound in a 29 000 K ideal gas of particle mass M_{Xe} travels a distance small compared to the channel radius during that time.

Variations in R_0 occur naturally from shot-to-shot. Fig. 5(a) is a scatter plot of $B^2 M_{Xe} \propto E/Ln_0$ vs. R_0 for individual sparks in 20 and 42 bar xenon, all at 5 kV and 170 μm electrode distance. From this plot, we find that,

$$\frac{E}{Ln_0} \propto B^2 M_{Xe} = K(R_0 - R_{min}), \quad (4)$$

with $K = 870(830) \pm 25(30) \text{ eV } \mu\text{m}$ and $R_{min} = 10(9) \pm 1(1) \mu\text{m}$ for 20(42) bar. Remarkably, $B^2 M_{Xe}$ is linear in R_0 and density-independent within experimental error. The spark brightness vs. initial radius shown in Fig. 5(b) emphasizes that the surface temperature, and by extension the energy/nucleus at the surface, is independent of the spark size in the brightness saturation regime.

These results considerably restrict models of the internal structure of the spark channel at the end of the ionization wave phase (~ 3 ns), after the energy has been deposited, but before hydrodynamic expansion has begun. The simplest consistent model is a shell structure with an energetically hollow core, and constant energy per nucleus ϵ_0 within a

shell of thickness Δ , i.e.,

$$\epsilon(r) = \begin{cases} \epsilon_0 & R_0 - \Delta < r < R_0 \\ 0 & \text{otherwise} \end{cases}, \quad (5)$$

$$\text{and } \bar{\epsilon} = \frac{2\Delta\epsilon_0}{R_0^2} \left(R_0 - \frac{\Delta}{2} \right). \quad (6)$$

Comparing Eqs. 2&4 with Eq. 6 yields the shell thickness $\Delta = 2R_{min}$ and energy per nucleus $\epsilon_0 = K/4\pi f(\gamma)R_{min}$, which is independent of R_0 as required for consistency with Fig. 5(a). Such a structure might arise when a moderately-conducting spark leader bridges the electrode gap, followed by a rush of current that is confined within an electrical skin depth. Heating within the skin-depth increases the conductivity of the shell relative to the rest of the channel, so that the shell draws the majority of the current density. At later times, this shell can spread inwards due to thermal conduction and radiation transport. Although γ is not strictly a fixed quantity, it is typically treated as a constant value of ~ 1.2 (consistent with 2 levels of ionization) for spark discharges and dense plasmas [1, 17, 19–21]. With this value of γ , the linear fit coefficients yield $\epsilon_0 = 14.4$ (15.3) \pm 1.3 (1.2) eV/nucleus for 20 (42) bar discharges.

To better understand these observations, it is necessary to consider the state of matter associated with the initial spark plasma. In this dense regime, screening effects and interparticle forces are dominant and can lead to unexpectedly high levels of ionization [1, 2, 9, 19, 22]. To determine whether this plasma is strongly ionized, the electron density can be estimated using the requirements for opacity [1, 2, 23, 24]. The absolute spectral intensity I_λ at wavelength λ can be calculated using [25],

$$I_\lambda = I_p (1 - \mathbb{R}) \frac{1 - \exp(-\kappa_\lambda l)}{1 - \mathbb{R} \exp(-\kappa_\lambda l)}, \quad (7)$$

where I_p is the Planck spectrum at T_{sat} , \mathbb{R} is the plasma reflectivity, $l = 2\Delta$ is the plasma thickness, and $\kappa_\lambda(T_{sat}, n_0, Z)$ is the absorption coefficient, where Z is the ionization level. Using the plasma conditions for 20 bar at 3 ns ($T_{sat} = 29\,000$ K and $l = 40\ \mu\text{m}$) and the free-free bremsstrahlung formula for κ_λ [23] with dense screening corrections [26], 2 levels of ionization is required to match the observed spectrum (Fig. 3). In contrast, the ionization calculated using Saha's equation in the dilute limit gives $Z = 0.3$ and cannot reproduce the plasma opacity. The high level of ionization potential reduction required is estimated by comparing the energy to ionize and heat these free electrons with $\epsilon_0 = 15$ eV/nucleus. Using

$Z = 2$, the thermal energy is $\frac{3}{2} (Z + 1) kT_{sat} = 11$ eV/nucleus. The vacuum ionization energy is $\sum_{i=1}^Z \chi_i = 33$ eV, giving a total of 44 eV/nucleus. Therefore, a dramatic reduction in the ionization potential must occur. Although formulated in a perturbative limit, the Debye screening formula suggests significant ionization potential lowering given by $\chi_D = -3e^2/\delta_D$, where $\delta_D = \sqrt{kT/24\pi e^2 n_0}$ is the Debye length and all atoms are assumed doubly-ionized [17]. For the parameters given above, $\Delta\chi = -20$ eV/nucleus, leaving a significantly lowered total energy of 24 eV/nucleus.

Our measurement of ionization potential lowering makes this system a platform for studying the equations of state and transport properties of strongly correlated plasmas. The plasma studied in this Letter is a robust state of matter, as the saturation temperature and opacity is maintained long after the input energy has ceased. Further study of dense plasmas on rapid timescales will lead to discoveries of exotic phases of gaseous coulombic systems that parallel unusual phases seen in liquid electrolytes [27] as a result of strong screening [28]. Due to its opacity, the screened plasma phase generated by spark discharges will make an excellent sub-nanosecond means of switching off ultra-violet probes, so as to make improved measurements for the state of trapped ion Q-bits [29, 30]. Other unexpected properties and applications of condensed plasmas remain to be discovered.

We gratefully acknowledge support from the Air Force Office of Scientific Research and the DARPA MTO for research on microplasmas.

* Electronic address: awbatal1@ncsu.edu

- [1] M. Skowronek, Phys. Fluids **13**, 378 (1970).
- [2] A. Bataller, G. R. Plateau, B. Kappus, and S. Putterman, Phys. Rev. Lett. **113**, 075001 (2014).
- [3] I. Model, Sov. Phys. JETP **5** (1957).
- [4] M. Liverts and N. Apazidis, Phys. Rev. Lett. **116**, 014501 (2016).
- [5] G. Vazquez, C. Camara, S. Putterman, and K. Weninger, Optics Letters **26**, 575 (2001).
- [6] G. Glaser, Optik **7**, 33 (1950).
- [7] G. Glaser, Z. Naturforschung A Phys. **6**, 706 (1951).
- [8] M. P. Vanyukov and A. A. Mak, Phys. Usp. **1**, 137 (1958).
- [9] U. Yusupaliev, Bull. Lebedev Phys. **34**, 264 (2007).

- [10] A. Bataller, J. Koulakis, S. Pree, and S. Putterman, *Appl. Phys. Lett.* **105**, 223501 (2014).
- [11] U. Yusupaliev, *Bull. Lebedev Phys.* **36**, 44 (2009).
- [12] F. Frungel, *Optik* **3**, 128 (1948).
- [13] M. P. Vanyukov and A. A. Mak, *Dokl. Akad. Nauk SSSR* **123** (1958).
- [14] H. Fischer and L. Michel, *Appl. Opt.* **6**, 935 (1967).
- [15] E. M. Bazelyan and Y. P. Raizer, *Spark Discharge* (Taylor & Francis, 1977), ISBN 0-8493-2868-3.
- [16] S. P. Bugaev, E. A. Litvinov, G. A. Mesyats, and D. I. Proskurovskii, *Sov. Phys. Usp.* **18**, 51 (1975).
- [17] Y. P. Zel'dovich, Ya. B., Raizer, *Physics of Shock Waves and High-temperature Hydrodynamic Phenomena* (Dover Publications, 1966), ISBN 0-486-42002-7.
- [18] L. I. Sedov, M. Friedman, M. Holt, and J. D. Cole, *J. Appl. Mech.* **28**, 159 (1961).
- [19] E. A. Martin, *J. Appl. Phys.* **31**, 255 (1960).
- [20] R. Drake, *High-Energy-Density Physics: Fundamentals, Inertial Fusion, and Experimental Astrophysics* (2006), ISBN 9783540293149.
- [21] U. Yusupaliev, *Bull. Lebedev Phys.* **37**, 71 (2010).
- [22] Z. Wen-Juan and A. Yu, *Chin. Phys. B* **24**, 47802 (2015).
- [23] A. Bataller, B. Kappus, C. Camara, and S. Putterman, *Phys. Rev. Lett.* **113**, 024301 (2014).
- [24] B. Kappus, A. Bataller, and S. Putterman, *Phys. Rev. Lett.* **111**, 234301 (2013).
- [25] G. Bekefi and S. C. Brown, *Am. J. Phys.* **29**, 404 (1961).
- [26] G. Dimonte and J. Daligault, *Phys. Rev. Lett.* **101**, 135001 (2008).
- [27] J. Jacob, M. A. Anisimov, A. Kumar, V. A. Agayan, and J. V. Sengers, *Int. J. Thermophys.* **21** (2000).
- [28] V. A. Kozlov, S. V. Sokolova, and N. A. Trufanov, *Sov. Phys. JETP* **71** (1990).
- [29] A. H. Myerson, D. J. Szwer, S. C. Webster, D. T. C. Allcock, M. J. Curtis, G. Imreh, J. A. Sherman, D. N. Stacey, A. M. Steane, and D. M. Lucas, *Phys. Rev. Lett.* **100** (2008).
- [30] J. Mizrahi, B. Neyenhuis, K. G. Johnson, W. C. Campbell, C. Senko, D. Hayes, and C. Monroe, *Appl. Phys. B* **114**, 45 (2014).
- [31] Considering that the speed of sound is much less than the ionization wave velocity, picking R_0 at a late time results in a small error compared to picking R_0 at too early in time. Therefore we prefer to err on the late side.